GEOSTANDARDS and GEOANALYTICAL RESEARCH

Towards a Higher Comparability of Geothermometric Data Obtained by Raman Spectroscopy of Carbonaceous Material. Part 2: A Revised Geothermometer

N. Keno **Lünsdorf** (1)*, István **Dunkl** (1), Burkhard C. **Schmidt** (2), Gerd **Rantitsch** (3) and Hilmar von **Eynatten** (1)

(1) Department of Sedimentology and Environmental Geology, Georg-August-Universität Göttingen, Göttingen, D-37077, Germany
(2) Department of Experimental and Applied Mineralogy, Georg-August-Universität Göttingen, Göttingen, D-37077, Germany
(3) Department of Applied Geosciences and Geophysics, Montanuniversität Leoben, Leoben, A-8700, Austria
* Corresponding author. e-mail: kluensd@gwdg.de

The estimation of the peak metamorphic temperature by Raman spectroscopy of carbonaceous material (RSCM) is influenced by several bias sources grouped in measuring conditions, spectral processing and sample heterogeneity. The measuring conditions (selected excitation wavelength) and the operator bias during spectral processing have a pronounced impact on the temperature estimate and thus on the comparability and portability of thermometric data obtained by RSCM. Several calibration lines of RSCM geothermometers are published already, but no standardised approach exists. Samples of carbonaceous material bearing metasediments with well-established metamorphic conditions of the central and western Alps compile a reference series. By applying an automated, iterative and randomised curve-fitting approach, a consistent and user input-independent RSCM geothermometer is presented, which covers peak metamorphic temperatures from *ca.* 160 to 600 °C. The method is hardware independent because the measuring conditions bias is excluded by the use of the reference series and the automated curve-fitting approach reduces the spectral processing bias effectively, increasing the method's comparability and portability. By distributing the reference series and the automated curve-fitting software, a laboratory will be able to derive a laboratory specific calibration line for the RSCM geothermometer.

Keywords: Raman spectroscopy, geothermometry, organic matter, reference sample series, metamorphic petrology.

Received 23 Mar 17 – Accepted 07 Jun 17

Raman spectroscopy of carbonaceous material (RSCM) characterises the transformation of immature organic matter to crystalline graphite, which mainly depends on temperature (Beyssac *et al.* 2002). Because this transformation is irreversible, RSCM is used to derive the peak metamorphic temperature of metasediments containing organic matter (e.g., Rahl *et al.* 2005, Beyssac *et al.* 2007, Wiederkehr *et al.* 2011, Scharf *et al.* 2013). The most widely used temperature range is about 330–650 °C (Beyssac *et al.* 2002), but attempts have been made to expand this range to diagenetic temperatures (e.g., Rahl *et al.* 2005, Lahfid *et al.* 2010, Kouketsu *et al.* 2014). Furthermore, the RSCM method is easily applicable and nondestructive, requires little sample preparation and thus is frequently applied in organic petrology studies, in which it is commonly correlated with organic maturity (Liu *et al.* 2013, Hinrichs *et al.* 2014, Wilkins *et al.* 2014, Rantitsch *et al.* 2016).

Different empiric calibrations exist to relate RSCM spectra to peak temperature (e.g., Beyssac *et al.* 2002, Rantitsch *et al.* 2004, Rahl *et al.* 2005, Aoya *et al.* 2010, Lahfid *et al.* 2010, Kouketsu *et al.* 2014). Usually, the calibration curves of RSCM geothermometers or the correlation of RSCM data to reflectance values depend on a specific evaluation scheme of the acquired Raman spectra and therefore many protocols for spectral evaluation exist. These often consist of a baseline subtraction, followed by curve fitting, using varying numbers (2–9) of Gauss, Lorentz, Voigt, pseudo-Voigt or Breit-Wigner-Fano functions to describe the intensity distribution in the recorded spectrum

doi: 10.1111/ggr.12178

(Kelemen and Fang 2001, Beyssac *et al.* 2002, Sadezky *et al.* 2005, Li *et al.* 2006, Quirico *et al.* 2009, Lahfid *et al.* 2010, Liu *et al.* 2013, Hinrichs *et al.* 2014, Kouketsu *et al.* 2014, Wilkins *et al.* 2014). The results of these procedures are often parameter ratios, like the R1, R2, RA1 and RA2 ratios after Beyssac *et al.* (2002) and Lahfid *et al.* (2010), that compare intensity, width or area values of the fitted functions. Many of these protocols require manual intervention during baseline estimation. All function parameters derived during curve fitting depend on this estimation, and thus, subjectivity is introduced during the spectral processing. According to Lünsdorf *et al.* (2014), the personal fitting strategy (operator bias) belongs to the spectral processing bias that represents one of three bias sources in RSCM studies. The operator bias can lead to significant differences in estimated temperatures, with respect to the used curve-fitting protocol. Lünsdorf *et al.* (2014) showed that the operator bias amounts up to 60 °C for the RA1 ratio after Lahfid *et al.* (2010) and up to 12 °C for the R2 ratio after Beyssac *et al.* (2002), when the same spectral data are evaluated by different operators. The other two sources of error are due to sample heterogeneity and due to different analytical conditions, including the used Raman devices, in which the excitation wavelength is of prime importance. Lünsdorf *et al.* (2014) concluded that a standardised, automatic curve-fitting routine would rule out the operator bias and that a reference sample series would allow each laboratory to create their own calibration curve, which decreases bias due to different instrumental set-ups, and therefore, the overall comparability of RSCM temperature information increases.

To provide a standardised approach to a revised RSCM geothermometer, this study aims at introducing a reference sample series, which is then combined with the automated curve-fitting routine 'Iterative Fitting of Raman Spectra – IFORS', presented in Lünsdorf and Lünsdorf (2016). Samples were collected in the central and western Alps at locations with well-established metamorphic conditions. The proposed reference series covers a peak temperature range of *ca.* 160–600 °C, that is, from deep burial to lower amphibolite facies metamorphic conditions. In this temperature range, the evolution of CM Raman spectra is complex and none of the published evaluation approaches describes this evolution continuously or without user guidance. Hence, an automated, operator-independent approach is presented that is based on the scaled total area-RSCM (STA-RSCM) method of Lünsdorf (2016) and Lünsdorf and Lünsdorf (2016).

Samples

To compile a reference series, sample locations were selected which adhere to the following rules with decreasing priority: (a) independent and well-constrained peak metamorphic temperature, (b) unweathered character (c), CM Raman spectra should be homogeneous in the sample, (d) accessibility of the sampling location. The samples were collected across the central and western Alps (Figure 1) and are categorised into three groups (Table 1). The first group represents the low temperature branch of the sample series and was collected in the Northern Helvetic Flysch units of the Glarus Alps and in the Helvetic units along the pyrophyllite-in

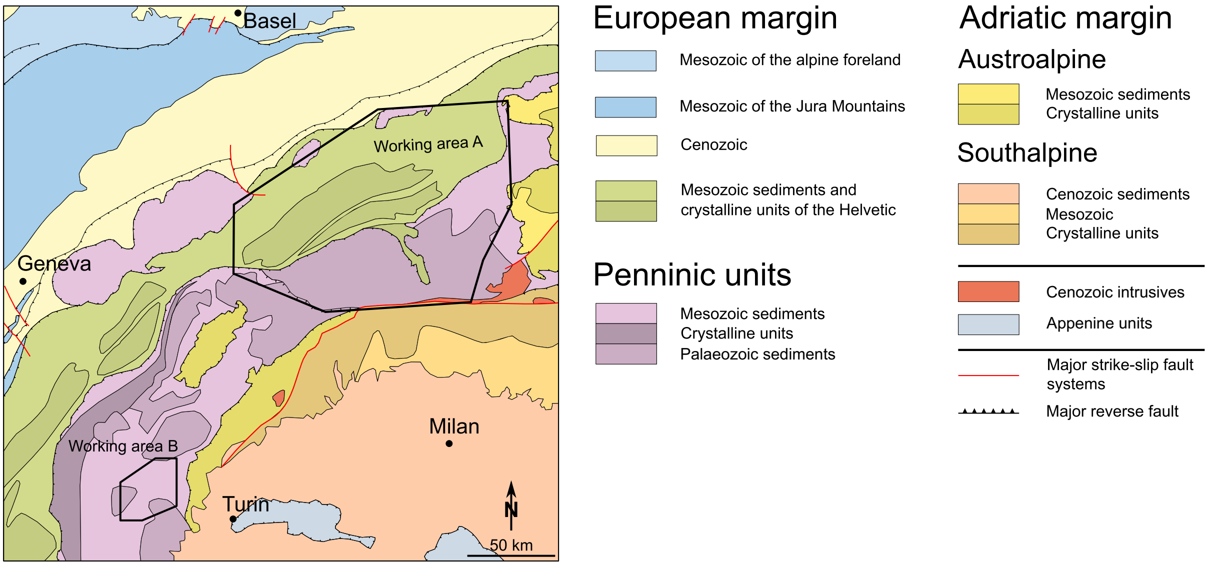

Figure 1. Simplified geological map of the sampled regions (after Pfiffner 2010). [Colour figure can be viewed at wileyonlinelibrary.com]

Table 1.
Details of the reference sample set

Sample	Rock type	Sample group	Lat.	Long.	Peak temp. (°C)	STA$_{488}$ nm	1*s*	STA$_{532}$ nm	1*s*	*N*	Method	Ref.
KL14_5	Pelite	1	47.1405	9.10165	162 ± 30*	241.0	5.4	230.8	7.9	28	2	A
KL14_7	Pelite	1	47.11788	9.00371	178 ± 30*	230.2	13.7	223.7	8.0	25	2	A
KL14_21	Silty pelite	1	46.9617	9.09306	228 ± 30*	223.0	10.8	221.9	5.3	20	2	A
KL14_16	Pelite	1	46.97697	9.05716	236 ± 30*	216.9	7.2	213.6	13.3	30	2	A
KL16_31	Marl	1	47.11033	9.44794	236 ± 30*	196.8	10.7	198.7	11.4	30	2	B
KL16_35	Pelite	1	47.0344	9.09412	240 ± 30*	204.4	6.8	202.2	7.5	30	2	B
KL14_17	Pelite	1	46.94665	9.03288	256 ± 30*	177.2	4.1	173.5	3.2	30	2	A
KL16_43	Pelite	1	46.51734	7.7493	262 ± 30*	180.7	6.7	174.8	6.3	30	2	B
KL14_13	Pelite	1	46.9669	9.171	267 ± 30*	172.9	5.6	167.9	4.8	30	2	A
KL14_1	Silty pelite	1	46.85627	9.10359	295 ± 20	132.5	3.8	127.4	2.9	30	1	A
KL14_19	Silty pelite	1	46.88838	9.04286	299 ± 23	162.1	2.7	153.1	2.2	27	1	A
KL16_8	Meta-marl	2	44.97242	6.85448	325 ± 25	106.3	9.2	112.5	6.9	20	4	E
KL16_19	Marble	2	44.98675	6.87342	350 ± 25	87.4	4.7	87.3	5.6	15	4	E
KL16_10	Marble	2	45.02926	6.89736	375 ± 35	79.4	2.6	71.0	3.8	15	4	E
KL16_11	Marble	2	45.0331	6.91046	375 ± 35	74.9	2.4	75.6	4.5	20	4	E
KL14_58	Calcareous mica-schist	3	46.646578	9.448071	370 ± 50	78.8	4.4	76.8	4.3	20	3	C
KL16_14	Meta-marl	2	45.06127	6.96675	415 ± 35	68.4	7.5	81.4	4.5	21	4	E
KL16_29	Meta-marl	3	46.56221	9.35223	420 ± 30	71.5	7.3	69.7	3.9	20	3	C
KL14_59	Calcareous mica-schist	3	46.67832	9.44969	420 ± 50	56.1	6.0	69.8	11.0	15	3	C
KL16_27	Marble	3	46.55367	9.23969	440 ± 30	37.7	5.4	53.1	5.5	20	3	C
KL14_56	Calcareous mica-schist	3	46.546089	9.279393	450 ± 30	42.1	4.2	57.2	5.0	20	3	C
KL16_23	Marble	3	46.43464	9.21321	480 ± 40	30.8	2.5	36.4	3.7	20	4	C/D
KL16_15	Marble	2	45.06413	7.0562	490 ± 40	38.8	4.7	45.4	9.8	19	4	E
KL16_16	Meta-marl	2	45.052905	7.063419	490 ± 40	28.5	4.0	35.7	5.5	10	4	E
KL14_52	Calcareous mica-schist	3	46.40111	9.228	520 ± 25	28.1	3.2	28.8	4.5	20	3, 4	C/D
KL14_49	Calcareous mica-schist	3	46.477916	8.724217	610 ± 50	21.5	2.4	23.4	3.5	20	3, 4	C/D

Lat., Latitude; Long., Longitude; 1 = Chlorite thermometry; 2 = Fluid inclusion homogenisation temperature; 3 = Calcite-dolomite thermometry; 4 = Pressure-temperature estimation by multi-equilibrium calculation; A = Rahn (1996); B = Frey (1987b); C = this study; D = Todd and Engi (1997); E = Agard *et al.* (2001a). In the case of fluid inclusion homogenisation temperatures marked by an asterisk, only the analytical error was provided in the literature and thus a geological uncertainty of ± 30 °C is assumed, which is in the same order of magnitude as the other thermometers, that is, chlorite thermometry (Rahn 1996), calcite–dolomite thermometry (Ebert *et al.* 2007).

(Prl-in) reaction isograd (Figure 2; Frey 1987b). The second group was taken along a profile in the Schistes Lustrés units in the western Alps (Figure 3; Agard *et al.* 2001a). The third group was gathered in (meta-) sediments of the central Alps in Switzerland (the so-called Bündnerschiefer) and was extended by samples from the central Lepontine Alps (Figure 2). The second and third groups represent the high-temperature branch of the sample series.

Samples of the first group are organic-rich black slates and metapelites, which cover very low-grade to lower greenschist facies conditions (Frey 1987b, Rahn 1996, Ebert *et al.* 2007). The peak metamorphic temperatures in the Glarus Alps are well constrained by fluid inclusion thermobarometry, chlorite thermometry and calcite–dolomite (Cal-Dol) thermometry (Rahn 1996, Ebert *et al.* 2007) covering a temperature range of about 160–320 °C. The reaction kaolinite + quartz → pyrophyllite + water was mapped by Frey (1987b), and the pressure (*P*) – temperature (*T*) conditions along this isograd were determined by fluid inclusion thermobarometry to 240–260 °C at about 1.5–2 kbar (Frey 1987b). For the reference series, eight samples were selected in the Glarus Alps and three samples along the Prl-in isograd (Figure 2).

Calcareous black schists and marbles of the Schistes Lustrés, also sampled by Beyssac *et al.* (2002), assemble the second group. The sediments of the Schistes Lustrés were deposited during Early Jurassic to Mid-Cretaceous times in the Piemont-Liguran trough (Lemoine *et al.* 1986, Deville *et al.* 1992) and experienced prograde blueschist to eclogite facies metamorphism followed by exhumation

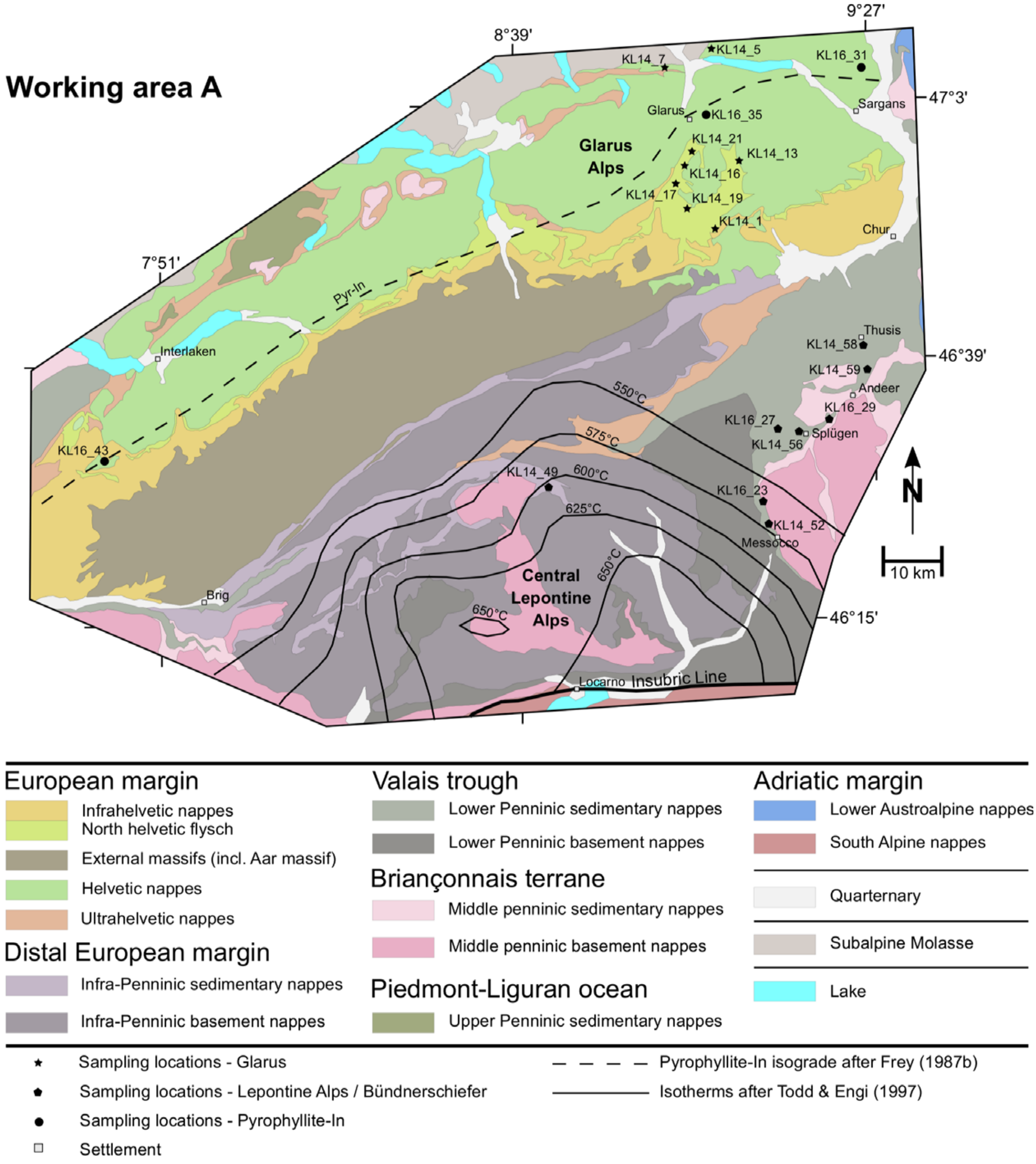

Figure 2. Simplified map of the tectonic units in the working area A (Figure 1). The sample locations are shown together with the Prl-in isograd (Frey 1987b) and the isotherms of the Lepontine dome (Todd and Engi 1997). The 'Bündnerschiefer (meta-) sediments' of sample group 3 belong to the Lower Penninic sedimentary nappes of the Valais trough (map-base after Swisstopo 2005). [Colour figure can be viewed at wileyonlinelibrary.com]

under greenschist facies conditions (Agard *et al.* 2001a). Agard *et al.* (2001a, b, 2002) provided *P-T* conditions from 300 to 350 °C at 12–13 kbar to 450–530 °C at 20–21 kbar, continuously increasing from W to E. A profile consisting of seven samples was collected along this *P-T* gradient (Figure 3).

Samples of the third group were collected along a profile from Mesocco to Thusis (Figure 2). They belong to the Bündnerschiefer of the central Alps and consist of metamorphosed, mostly Cretaceous, hemipelagic-turbiditic pelites, marls and sandy limestones deposited in the northern Penninic Valaisan trough (Steinmann 1994). Peak

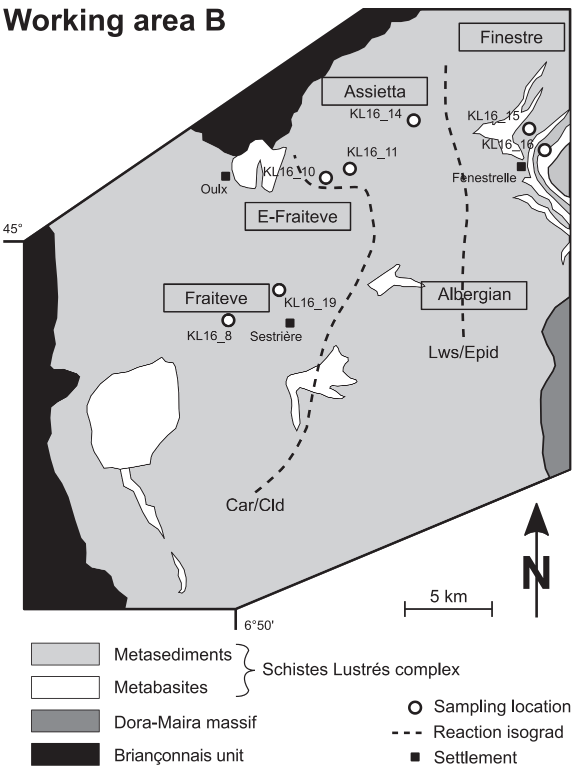

Figure 3. Simplified geological map of working area B (Figure 1) with sampling locations; see Table 1 for accurate co-ordinates (after Agard *et al.* 2001a).

metamorphic conditions in the Bündnerschiefer reached 350–400 °C and 12 to 14 kbar during a subduction related *HP-LT* event (Bousquet *et al.* 2002, Wiederkehr *et al.* 2008). Rapid isothermal decompression followed under lower greenschist facies conditions. Wiederkehr *et al.* (2009) dated the *HP-LT* event to *ca.* 41 Ma. Metamorphic conditions decrease in the Bündnerschiefer towards the NE. In the SW of the Bündnerschiefer profile, the *HP-LT* event has been overprinted by a Barrovian-type thermal event, reaching amphibolite facies conditions that lead to the present-day distribution of isotherms in the Lepontine Alps (Todd and Engi 1997, Wiederkehr *et al.* 2009). In general, peak metamorphic temperatures in the Lepontine area increase from *ca.* 500 °C in the peripheral parts to *ca.* 675 °C in the central parts near the Insubric Line (Figure 2, Todd and Engi 1997, Frey and Ferreiro Mählmann 1999). Wiederkehr *et al.* (2009) dated the Barrovian-type overprint to *ca.* 19–18 Ma. To complete the high-temperature branch of the reference series, an additional sample (KL14_49) was collected in the central Lepontine Alps in the Lebendun Nappe at Lake Tremorgio where a peak metamorphic temperature of about 600 °C has been determined. All sample locations are listed in Table 1 together with their associated temperature and the used geothermometers.

Methods

Samples of group one were prepared as polished blocks. The polished surface is needed to identify CM grains (i.e., vitrinite, inertinite and bituminite), which is important for diagenetic to very low-grade samples. The molecular structure of metamorphic CM alters during polishing (Wopenka and Pasteris 1993, Beyssac *et al.* 2003, Crespo *et al.* 2006, Ammar and Rouzaud 2012), which leads to increasing D-band intensities and ultimately to false temperature information. However, Lünsdorf (2016) showed that Raman spectra of CM in samples from very low- to low-grade conditions are unaffected by polishing if the process is stopped after using a 1-μm diamond suspension. Therefore, samples of group one were prepared as blocks, cut perpendicular to bedding. Afterwards, the blocks were ground and polished by 9-, 3- and 1-μm diamond suspension. The samples of group two and three were prepared as thin sections, cut perpendicular to bedding. CM in these samples is partly graphitized or composed of microcrystalline graphite and to avoid alteration due to polishing, the CM grains were measured beneath a translucent mineral, as suggested by Beyssac *et al.* (2003).

Raman spectra were acquired with a Horiba Jobin Yvon HR800-UV and a Horiba Jobin Yvon XploRA Plus spectrometer. Both systems were set up in 180° backscattering geometry and used an Olympus BX-41 microscope. The focal length of the HR800-UV was 800 mm, and the instrumental set-up included a 488-nm diode laser, a 100× objective with 0.9 numerical aperture and a grating with 600 l mm^{-1}. The confocal hole diameter was set to 100 μm, and the recorded spectrum was centred at 1399.81 cm^{-1}. The focal length of the XploRA Plus was 200 mm, and the instrumental set-up included a 532 nm diode laser, a 100× objective with 0.9 numerical aperture and a grating with 1800 l mm^{-1}. The confocal hole diameter and slit width were set to 100 μm, and the recorded spectrum was centred at 1299.89 cm^{-1}.

The on-sample laser power was controlled by density filters to < 0.5 mW, and immature samples were checked for burn marks or photo-bleaching after each measurement. Both systems were calibrated against the 520.4 cm^{-1} line of silicon, and each recorded spectrum represents 3–5 accumulations of 10–90 s.

In the case of metamorphic samples (sample groups two and three), care was taken to measure CM grains in parts of the sample that showed an isotropic fabric. Obviously, strained parts, showing elongated grains, were excluded. This was done because Bustin *et al.* (1995) showed that strain energy promotes graphitization and Barzoi (2015) proved that even on the thin-section scale strain leads to differential graphitization and ultimately to temperature differences of up to 150 °C when the RSCM thermometer after Beyssac *et al.* (2002) is applied. Depending on the abundance of grains, 10–30 CM grains were measured per sample.

If not indicated otherwise, all results and figures discussed in the results refer to data obtained with the HR800-UV spectrometer using the 488-nm laser for excitation. The XploRA Plus system with the 532 nm laser was used to produce RSCM data that is directly comparable with published data in, for instance, Rahl *et al.* (2005), Aoya *et al.* (2010) and Kouketsu *et al.* (2014).

Calcite–dolomite thermometry was performed on selected samples (see Table 1). Metamorphic temperatures were calculated according to the Fe-corrected calibration given by equation 31 in Anovitz and Essene (1987) as most calcites contain iron. Analyses were carried out with a JEOL JXA-8900RL electron probe microanalyser. The beam diameter was set to 20 µm at 15 nA with an acceleration voltage of 15 kV.

Samples across the Prl-in isograd were analysed by X-ray powder diffractometry to verify the co-existence of pyrophyllite and kaolinite. XRD spectra were acquired using a Panalytical XPERT-MPD spectrometer with Cu-Kα radiation at 40 kV and 30 mA. A spectral range of 2–40° 2Θ with a step size of 0.02° 2Θ was recorded for 4 s per step.

Evaluation of Raman spectra

The Raman spectrum of CM is composed of two major intensity accumulations in the regions of 1000–1500 cm^{-1} and 1500–1700 cm^{-1}, named here the D- and G-band-region (Figure 4). The intensity distribution in these regions depends on the maturity stage or degree of graphitization and used excitation wavelength (Vidano *et al.* 1981, Wang *et al.* 1990, Wopenka and Pasteris 1993, Yui *et al.* 1996, Pócsik *et al.* 1998, Matthews *et al.* 1999, Ferrari and Robertson 2001, Castiglioni *et al.* 2004, Reich and Thomsen 2004, Pimenta *et al.* 2007). In none graphitized CM, the spectrum is made up of two strong bands centred at 1330–1370 cm^{-1} and 1590–1610 cm^{-1}, depending on maturity stage and used excitation wavelength. The band centred at 1330–1370 cm^{-1} shows additional shoulders on both sides (Figure 4a). Thus, the CM spectra of none graphitized CM are usually curve-fitted by five Lorentz functions (Lahfid *et al.* 2010) or a mixture of four Lorentz and one Gauss function (Sadezky *et al.* 2005); thus, several

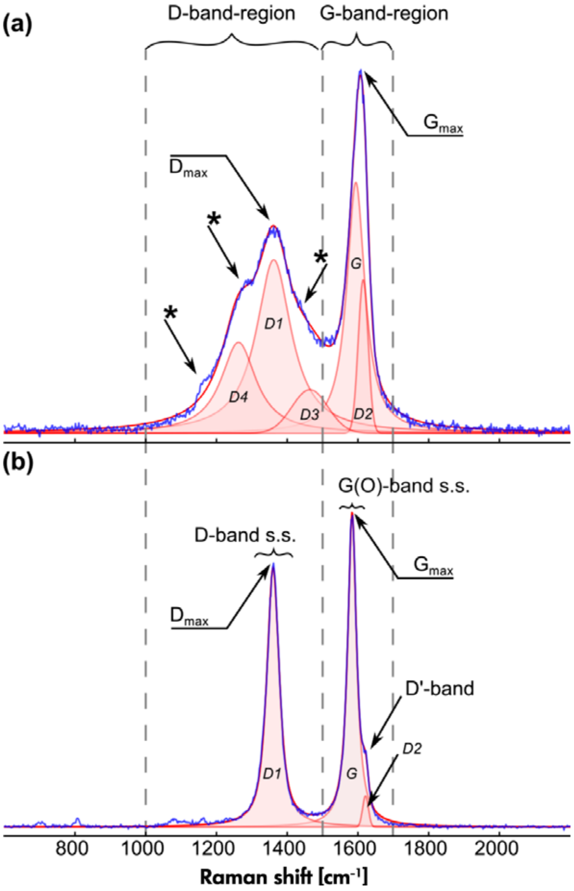

Figure 4. Nomenclature of CM Raman spectra. (a) A Raman spectrum of CM from very low-grade metamorphic conditions. The intensity is distributed in the D-band- and G-band-region, from 1000 to 1500 cm^{-1} and from 1500 to 1700 cm^{-1}, respectively. D_{max} and G_{max} refer to the maximum intensity value in D-band- and G-band-region. The D-band-region is characterised by a central Raman band containing D_{max}. This band is often decorated by additional shoulders on the low- and high-wavenumber side (indicated by the asterisks). Due to the additional shoulders, the D-band-region is generally curve-fitted by three functions, commonly labelled D1, D3 and D4 (Sadezky *et al.* 2005, Lahfid *et al.* 2010). The G-band-region consists of one broad Raman band containing G_{max}. This Raman band is frequently curve-fitted by two functions, commonly labelled D2 and G (Beyssac *et al.* 2002, Sadezky *et al.* 2005, Lahfid *et al.* 2010). (b) A Raman spectrum of graphitic CM. The intensity is also distributed in the D-band- and G-band-region, but here the D1 function suffices to describe the single Raman band in the D-band-region. This band is the D-band *sensu stricto*, meaning that it is induced by defects or disorder in the graphite lattice. In the G-band-region, the intensity is distributed between G(O)- and D′-band, with G referring to graphite and O to 'ordered'. The G- and D′-band are sufficiently described by the G- and D2-functions. [Colour figure can be viewed at wileyonlinelibrary.com]

functions are needed to describe the intensity distribution in the D-band- and G-band-region (Figure 4a). In the case of graphitic CM, the intensity distribution in the D-band- and G-band-region reduces to three distinct bands, the D-band (s.s.), the G-band (s.s.) and the D′-band (Figure 4b), and each band is commonly described by one Voigt function, namely the D1-, D2-, G-, and if present the D3-function (Beyssac *et al.* 2002, Rantitsch *et al.* 2016).

Instead of these 'classic' instructions (e.g., Beyssac *et al.* 2002, Sadezky *et al.* 2005, Lahfid *et al.* 2010), a different curve-fitting approach is chosen here because the classical ones are prone to operator bias (Lünsdorf *et al.* 2014). Consequently, the user input-independent software suite of Lünsdorf and Lünsdorf (2016) is used, which facilitates iterative, random-based curve fitting. The software simultaneously models the background and the Raman signal, approached by a fifth-order polynomial and pseudo-Voigt functions (PV), respectively. The model is given by the sum of the PV functions and the polynomial fitted to the spectrum by randomly changing a single function parameter [centre, height, half width at half maximum (HWHM), Gauss/Lorentz factor]. This optimisation process is partly guided, as the function parameters adhere to a set of constraints; that is, HWHM must stay below a maximum value and negative function values are not allowed (see Lünsdorf and Lünsdorf 2016 for details). The optimisation continues until a threshold value is reached. Then, the model is extended by another PV function. This iterative process repeats itself until no more PV functions can be added to the model. The sum of the optimised PV functions yields a curve, which is a smoothed, accurate, baseline-corrected representation of the spectrum from which the D_STA (Equation 1) and G_STA (Equation 2) parameters are computed, with STA being the abbreviation for scaled total area (Lünsdorf and Lünsdorf 2016):

$$\mathrm{D\_STA} = \frac{1}{D_{\max}} \sum_{i=1}^{k} \int_{1000}^{1800} D_{\mathrm{i}}^{\mathrm{PV}}(x)\,\mathrm{d}x \qquad (1)$$

$$\mathrm{G\_STA} = \frac{1}{G_{\max}} \sum_{i=1}^{k} \int_{1000}^{1800} D_{\mathrm{i}}^{\mathrm{PV}}(x)\,\mathrm{d}x \qquad (2)$$

where $D_{\mathrm{i}}^{\mathrm{PV}}$ is the intensity of the *i*th PV function evaluated at wavenumber *x*. These parameters represent the sum of all intensity values in the interval from 1000 to 1800 cm^{-1} of the spectral representation, with D_STA being scaled to the maximum value in the D-band-region ($D_{\max}$ in Figure 4a) and G_STA being scaled to the maximum value in the G-band-region ($G_{\max}$ in Figure 4a). D_STA reliably describes the evolution of dispersed organic matter Raman spectra during coalification and graphitization (Lünsdorf 2016, Lünsdorf and Lünsdorf 2016).

Additional Raman bands may be present in the spectrum when measuring through a translucent mineral. To exclude these bands, they need to be removed from the model. This is achieved by defining Raman shift intervals for the additional mineral Raman bands in the STA interval (1000–1800 cm^{-1}) and by removing any PV function with a centre value that coincides with mentioned intervals (Table 2). The list of intervals can be adjusted and extended by the user if other phases than the ones shown in Table 2 occur in the sample.

Results

Glarus Alps (Sample group one)

In the Glarus samples (Figure 5), D_STA decreases linearly with increasing temperature, while G_STA decreases and above *ca.* 270 °C increases again. The position of the maximum value in the D-band-region shifts significantly from 1350 cm^{-1} at *ca.* 180 °C to 1335 cm^{-1} at about 270 °C and increases with higher temperatures. The position of the maximum value in the G-band-region continuously decreases from *ca.* 1607 to 1602 cm^{-1}. The shift in the $D_{\max}$ position is related to selective resonance Raman spectra of differently sized polyaromatic layers in the turbostratic structure of the CM and reflects the growth of aromatic layers due to increasing temperature (Lünsdorf 2016). The $D_{\max}/G_{\max}$ intensity ratio is constant at *ca.* 0.6 for temperatures below 300 °C. Above 300 °C, this ratio increases to 0.8–1.0.

Frey (1987b) mapped the Prl-in isograd within the Helvetic Nappes (Figure 2) by coexisting kaolinite (Kln) and

Table 2.
Raman shift intervals of Raman bands of typical, rock-forming translucent minerals

Raman band interval (cm^{-1})	Mineral
1080–1093	Carbonate
1070–1080	Carbonate
1435–1445	Carbonate
1744–1760	Carbonate
1095–1105	Plagioclase
1110–1118	Plagioclase
1155–1165	Quartz
1060–1070	Quartz

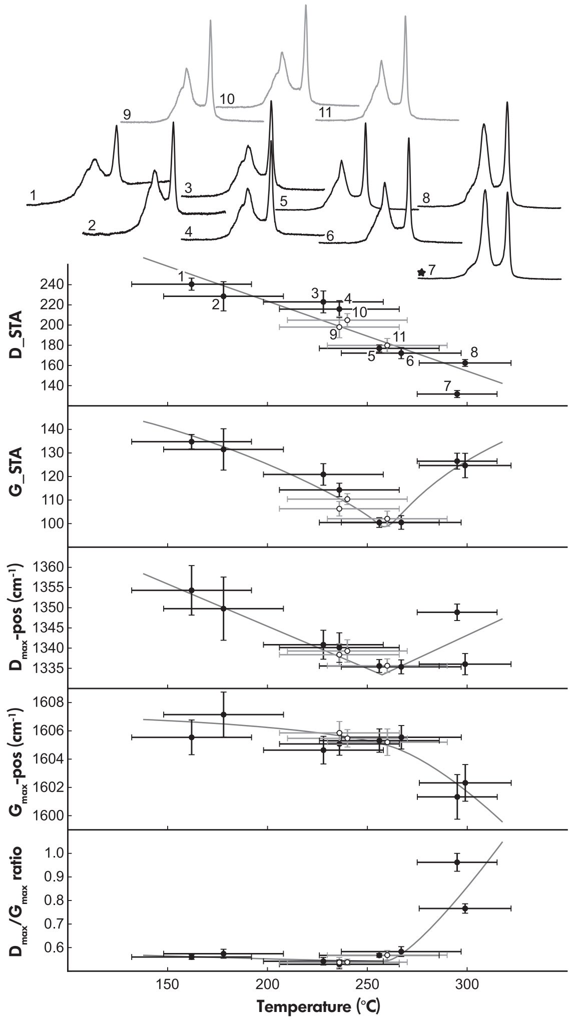

Figure 5. A compilation of the most indicative Raman parameters obtained on the samples from the Glarus Alps and across the pyrophyllite-in isograd. Representative spectra for each data point are shown at the top. Spectra of the Glarus profile are presented in black and spectra of the pyrophyllite-in isograd in grey. The numbers indicate which parameters are associated with each spectrum, and the star marks a spectrum that shows large deviation in the Raman parameter D_STA and the associated temperature information. The grey lines indicate the trends.

pyrophyllite. Three samples (KL16_31, KL16_35, KL16_43) were collected along this isograd (Figure 2, samples 51, 53, 54 in Frey 1987b). To verify the reaction Kln + Qz → Prl + H_2O, all three samples were analysed for pyrophyllite and kaolinite by XRD. Only in sample KL16_35, both minerals were found, while in the other neither pyrophyllite nor kaolinite was detected. Nevertheless, these samples are used because their proximity to the sampling locations of Frey (1987b) indicates similar metamorphic conditions. KL16_31 north of Sargans and KL16_35 east of Glarus show similar Raman parameters (D_STA *ca.* 200 ± 8) and Frey (1987b) reported a fluid inclusion homogenisation temperature of 236 °C for KL16_31 (i.e., sample 51 in Frey 1987b), while KL16_43 shows lower D_STA values (*ca.* 180 ± 7) and a higher homogenisation temperature of 262 °C. The linear correlation of D_STA and temperature of the Prl-in samples parallels the linear correlation of the Glarus samples. The Prl-in samples demonstrate that the STA approach is able to resolve relative temperature differences of at least 20 °C for CM that underwent low temperature metamorphism in the sense of Frey (1987a). The metamorphic temperature of sample KL14_1 (spectrum 7 in Figure 5) was estimated with 295 ± 20 °C by Rahn (1996) using chlorite thermometry based on the empirical calibration after Cathelineau (1988). The D_STA value suggests a higher temperature, which is supported by temperature estimates after Ebert *et al.* (2007) who provide Cal-Dol temperature values of 320–332 °C about 10 km to the north-east of the sampling location KL14_1. Furthermore, D_{max} is more intense than G_{max} (D_{max}/G_{max} ratio > 1; Figure 5), which indicates temperatures well above 300 °C.

Schistes Lustrés in the Western Alps (Sample group two)

A profile in the Schistes Lustrés of the Cottian Alps (Figure 3) covers metamorphic conditions of the low blueschist facies, 300–350 °C at 12–13 kbar at Fraiteve in the west, to the lower eclogite facies in the east at Finestre (450–530 °C at 20–21 kbar, Agard *et al.* 2001a, b, 2002). Agard *et al.* (2001a, 2002) provided average metamorphic conditions for five regions in the sampling area, that is Fraiteve, E-Fraiteve, Assietta, Albergian and Finestre (Figure 3). The pressure and temperature conditions increase continuously from west to east (Agard *et al.* 2001a) and the carpholite/chloritoid as well as the lawsonite (Lws)/epidote (Ep) isograds cross the profile in the eastern parts (Figure 3). The selected samples cover the regions of Fraiteve, E-Fraiteve, Assietta and Finestre and the central values of the *P-T* ellipses in Agard *et al.* (2001a) provide the temperature estimation with associated uncertainty. The sequence of CM Raman spectra shown in Figure 6 indicates a strong variability of the spectral shape along the profile, which is especially true for the Assietta where the second D_{max}/G_{max} inversion is observed (see section 'The STA geothermometer' and Figure 9). Thus, it is unreasonable to assume a single, averaged temperature for the Assietta. Samples KL16_10 and KL16_11 are situated in the western part of the Assietta and close to the Car/Cld isograd, while KL16_14 is situated in the eastern

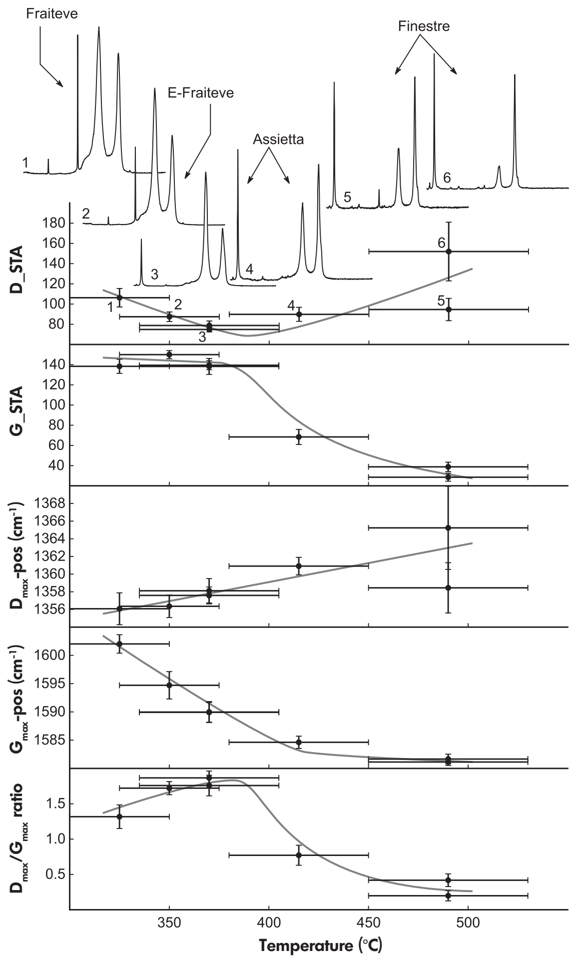

Figure 6. A compilation of the most indicative Raman parameters obtained from the Schistes Lustrés metasediments. Representative spectra for each data point are shown at the top. The additional sharp Raman bands in the spectra belong to calcite (*ca.* 1080 cm^{-1}) and quartz (*ca.* 464 cm^{-1}). The grey lines indicate the data trends.

part of the Assietta closer to the Lws/Ep isograd (Figure 3). Due to the Fe-Mg composition of carpholite (Car) and chloritoid (Cld), Agard *et al.* (2001b) deduced the reaction Car = Qz + Cld + water in a temperature range of 350–400 °C. Therefore, samples KL16_10 and KL16_11 are associated with 375 °C and an uncertainty of ± 35 °C, which is the temperature uncertainty provided for the Assietta-Albergian region in Agard *et al.* (2001a). For sample KL16_14, the average temperature and its associated uncertainty (415 ± 35 °C) of the Assietta-Albergian region of Agard *et al.* (2001a) are assumed, as this sample is situated to the west of the Lws/Ep isograd, which marks a temperature of 400–450 °C at 14 ± 2 kbar (Agard *et al.* 2001b).

Figure 6 shows that D_STA linearly decreases from 325 to *ca.* 400 °C and linearly increases above. G_STA values remain constant at *ca.* 145 from 325 to 375 °C, drop to *ca.* 65 at 415 °C and continue to decrease to *ca.* 35 at 490 °C. The maximum value in the D-band-region linearly shifts from 1356 cm^{-1} at 325 °C to 1364 cm^{-1} at 490 °C, while the maximum value in the G-band-region shifts from 1602 cm^{-1} at 325 °C to 1585 cm^{-1} at 415 °C and continuous to decrease to 1582 cm^{-1} at 490 °C. The D_{max}/G_{max} ratio increases from *ca.* 1.3 at 325 °C to *ca.* 1.8 at 375 °C, decreases to *ca.* 0.8 at 415 °C and continuous to decrease to *ca.* 0.3 at 490 °C.

Lepontine Alps and Bündnerschiefer (Sample group three)

In total, eight samples were collected in this area. Seven of them compose a profile in the Bündnerschiefer series from Mesocco to Thusis (Figure 2). Sample KL14_49 was collected in the central Lepontine Alps and provides the highest peak metamorphic temperature of the sample set. Although it does not belong to the Bündnerschiefer profile, it is included since KL14_52 and KL16_23 mark the transition from the Lepontine into the Bündnerschiefer units, at which the *HP-LT* metamorphic event was overprinted by Early Miocene Barrovian-type metamorphism (Wiederkehr *et al.* 2009). Thus, samples KL14_49, KL14_52 and KL16_23 represent the amphibolite facies conditions of the Barrovian event and the other samples indicate high to low blueschist facies conditions of the subduction related *HP-LT* event. From the bimodal distributions of the Mg-content in calcite (Figure 7), it is evident that most samples experienced retrograde overprint during exhumation (Dachs 1990). Consequently, average Cal-Dol temperatures underestimate the peak metamorphic temperature. However, the maximum Cal-Dol temperatures are in good agreement with the temperature gradient of Todd and Engi (1997), derived by multi-equilibrium calculation. Therefore, Cal-Dol$_{max}$ is used as a minimum peak metamorphic temperature estimate (Essene 1983). Because Cal-Dol$_{max}$ is a single value, its uncertainty is unknown and is therefore conservatively estimated by the sample standard deviation.

From 370 to 610 °C, D_STA linearly increases while G_STA exponentially decreases (Figure 8). In the same temperature interval, the maximum value in the D-band-region also increases linearly from 1358 to 1366 cm^{-1}, which is related to an increasing asymmetry of the D-band. The maximum value in the G-band-region shifts from 1590 cm^{-1} at 370 °C to *ca.* 1580 cm^{-1} at *ca.* 450 °C. The D_{max}/G_{max} ratio shows a similar trend as G_STA (Figure 8).

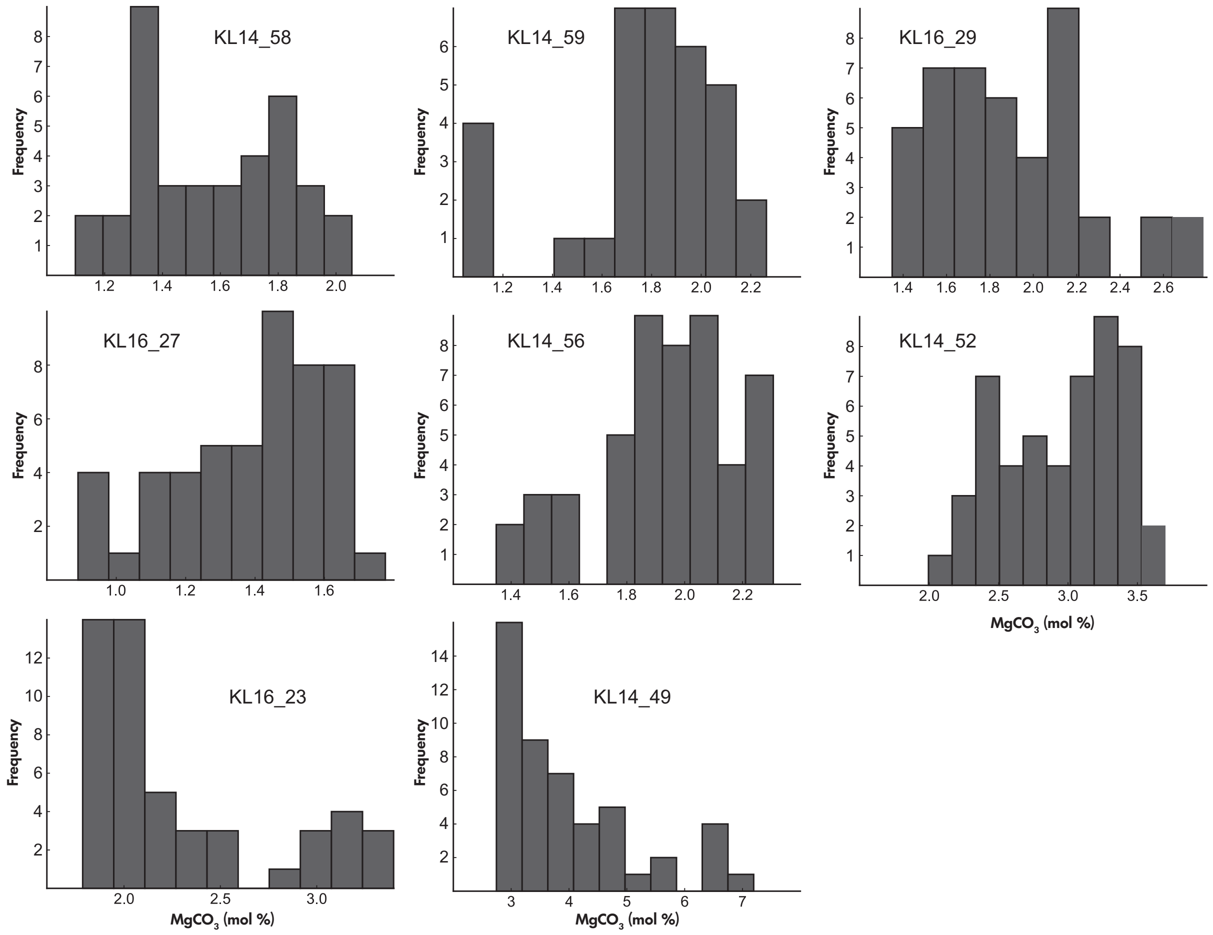

Figure 7. Histograms showing the distribution of $MgCO_3$ content in the calcites of the Bündnerschiefer and Lepontine Dome schists. The distributions are either bimodal or skewed, indicating the impact of retrograde overprint that resulted in partial re-equilibration of carbonates.

The STA geothermometer

The presented sample series covers deep burial to metamorphic temperatures from about 160 °C to *ca.* 600 °C. Figure 9 shows the composite trends in D_STA, G_STA, D_{max_pos}, G_{max_pos}, and the D_{max}/G_{max} ratio across the whole temperature range. They are separated into a low temperature zone, a transition zone and a high-temperature zone. All parameters change significantly in the transition zone between *ca.* 300 and 400 °C. This zone is marked by significant changes in the intensity ratios and positions of the maximum values in the G- and D-band-regions. Up to *ca.* 270 °C, D_{max} is always lower than G_{max} (D_{max}/G_{max} *ca.* 0.6) and the G-band-region is centred at *ca.* 1605 cm^{-1}. Between 300 and 375 °C, D_{max} increases and surpasses the value of G_{max}. This (first) intensity inversion (D_{max}/G_{max} ratio increases from values < 1 to values > 1) is correlated with a temperature of *ca.* 300–320 °C. D_{max} reaches its maximum intensity at *ca.* 375 °C (D_{max}/G_{max} *ca.* 1.8) and decreases to a D_{max}/G_{max} ratio of *ca.* 0.8 at 415 °C while passing through a second inversion point at about 400 °C, at which D_{max} becomes lower than G_{max} again. In the same temperature interval, the position of G_{max} shifts from *ca.* 1602 cm^{-1} to *ca.* 1585 cm^{-1}, the D′-band develops as a distinguishable shoulder on the G-band (s.s.) at *ca.* 1620 cm^{-1} and the D-band (s.s.) shifts to *ca.* 1360 cm^{-1}. All these characteristics are typical for Raman spectra of microcrystalline graphite recorded with an excitation wavelength of 488 nm (Tuinstra and Koenig 1970). Thus, after the transition zone, most of the CM has changed into microcrystalline graphite. The G_STA parameter passes through a maximum in the transition zone and decreases afterwards while the D_STA parameter continuously decreases to the end of the transition zone and increases again after the transition zone. Therefore, the thermometer can solely rely on the D_STA parameter. However, after the

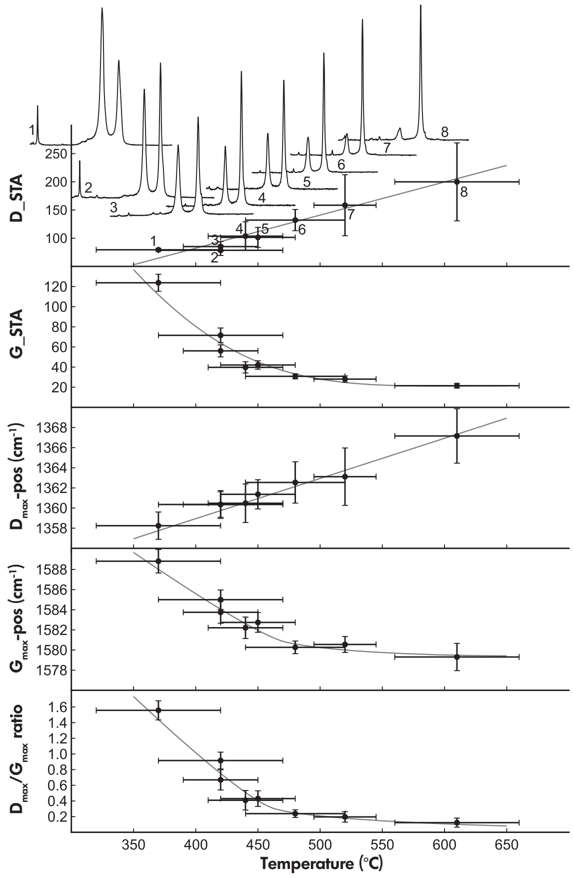

Figure 8. A compilation of the most indicative Raman parameters obtained from the Bündnerschiefer and Lepontine Alps samples (sample group three). Representative spectra for each data point are shown at the top. The additional sharp Raman bands in the spectra belong to calcite (*ca.* 1080 cm^{-1}) and quartz (*ca.* 464 cm^{-1}). The grey lines indicate the data trends.

second D_{max}/G_{max} inversion point, the spread of D_STA values for a given sample increases. This is because the intensity values are scaled to D_{max}, and thus, small intensity differences in D_{max} within a sample lead to over-amplification of the strong, relative intensity increase in the G-band-region. This over-amplification is avoided if the intensity values are scaled to G_{max}, that is, using the G_STA parameter. Up to the second D_{max}/G_{max} inversion point, this parameter does not produce a consistent correlation with temperature, while after the second D_{max}/G_{max} inversion point a negative, exponential correlation is evident (Figure 9).

A reliable parameter to decide which STA parameter to use is given by the G-shape-factor. It is the ratio of the average intensity value in the Raman shift interval from 1575 to 1595 cm^{-1} (G-band position *sensu stricto*) divided by the average intensity value in the Raman shift interval from 1610 to 1630 cm^{-1} (D′-band):

$$\text{G\_shape\_factor} = \frac{\frac{1}{(b-a)G_{max}}\sum_{i=1}^{k}\int_{a}^{b} D_{i}^{PV}(x)\mathrm{d}x}{\frac{1}{(d-c)G_{max}}\sum_{i=1}^{k}\int_{c}^{d} D_{i}^{PV}(x)\mathrm{d}x} \qquad (3)$$

where D_i^{PV} is the intensity of the *i*th PV function evaluated at wavenumber x, a = 1575 cm^{-1}, b = 1595 cm^{-1}, c = 1610 cm^{-1} and d = 1630 cm^{-1}. It describes the characteristic progression of the intensity distribution in the G-band-region from *ca.* 160 °C to *ca.* 600 °C (Figure 10). From *ca.* 160 ° to *ca.* 300 °C, the intensity distribution is roughly symmetric with G_{max} situated at 1600–1610 cm^{-1}, resulting in a G-shape-factor of about 1. Neither the G-band, nor the D′-band can be resolved properly in the G-band-region in this temperature interval. At about 350 °C, the maximum intensity in the G-band-region shifts towards lower relative wavenumbers and the D′-band becomes visible, which is marked by increasing G-shape-factor values. After the second D_{max}/G_{max} inversion point is reached at about 400 °C, the maximum intensity value in the G-band region stays at the G-band (s.s.) position (i.e., 1582 cm^{-1}). With increasing temperature, the intensity distribution in the G-band-region becomes narrower and the average intensity value in the D′-band interval decreases which results in increasing G-shape-factor values (Figure 10).

In Figure 11a, the G-shape-factor, D_STA and G_STA are plotted against the metamorphic temperature estimates. Up to temperatures of about 350 °C, the G-shape-factor remains constant at *ca.* 1. Above 350 °C, the G-shape-factor increases steeply and the slope maximises in the temperature interval between *ca.* 370 and 450 °C. From 450 to 600 °C, the slope decreases and remains constant. Close before the second D_{max}/G_{max} inversion (*ca.* 380 °C), D_STA is at its minimum (*ca.* 75), G_STA is at its maximum (*ca.* 150) and the slope of the G-shape-factor begins to increase. After this interval at about 420 °C, the slope of the G-shape-factor increases, G_STA drops to *ca.* 70 and D_STA rises to *ca.* 80. These significant changes in parameters are related to the second D_{max}/G_{max} inversion. It is also evident that G_STA and D_STA give similar values at the second D_{max}/G_{max} inversion. Because the intensity in the D-band-region gradually decreases after this inversion point, G_STA also decreases, while D_STA increases (Figure 11a). Using the G-shape-factor, spectra that have crossed the second D_{max}/G_{max} inversion are identified. Spectra at the

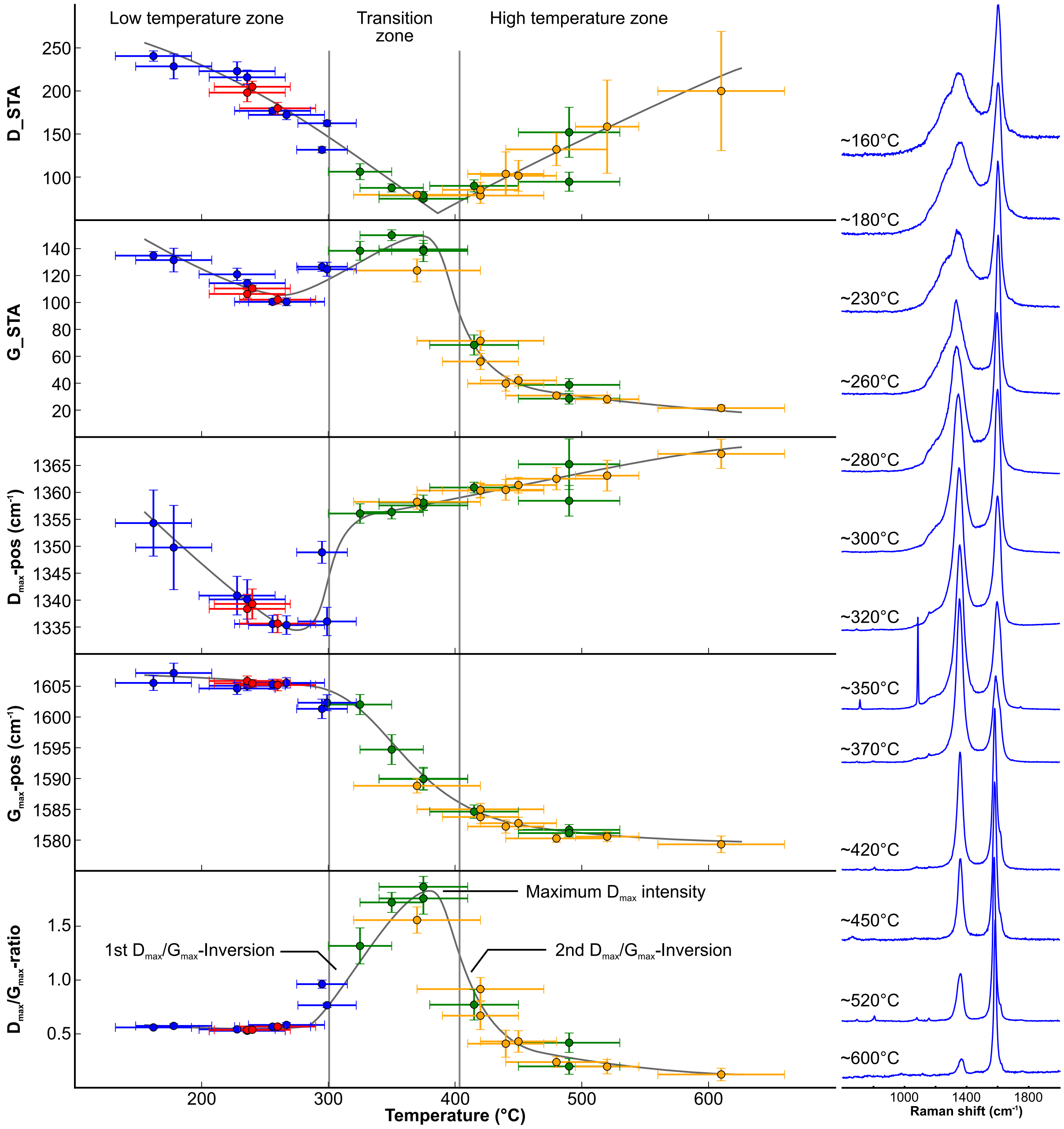

Figure 9. A compilation of the results of the complete reference sample series. Representative spectra of the temperature intervals are shown on the right. Every parameter plotted changes in the transition zone except D_STA. Blue/filled circles: Glarus Alps samples, red/filled circles Prl-in samples, green/filled circles: Schistes Lustrés samples, yellow/filled circles Lepontine Alps and Bündnerschiefer samples. The grey lines indicate the data trends. [Colour figure can be viewed at wileyonlinelibrary.com]

second inversion point, with a D_{max}/G_{max} ratio of about 1, a present D′-band and a G_{max} at *ca.* 1585 cm^{-1}, show G-shape-factors greater than ~3. Hence, the threshold for the G-shape-factor is set to 3 (Figure 11a). This concept allows to connect the D_STA values of the low temperature and transition zones with the G_STA values of the high-temperature zone, resulting in a regression of continuously decreasing STA values from *ca.* 160 to *ca.* 600 °C (Figure 11b).

Since green lasers (514.5 and 532 nm) are frequently used in RSCM studies, the STA values of CM spectra acquired with the XploRA Plus spectrometer (532 nm) are plotted for comparison in Figure 11b.

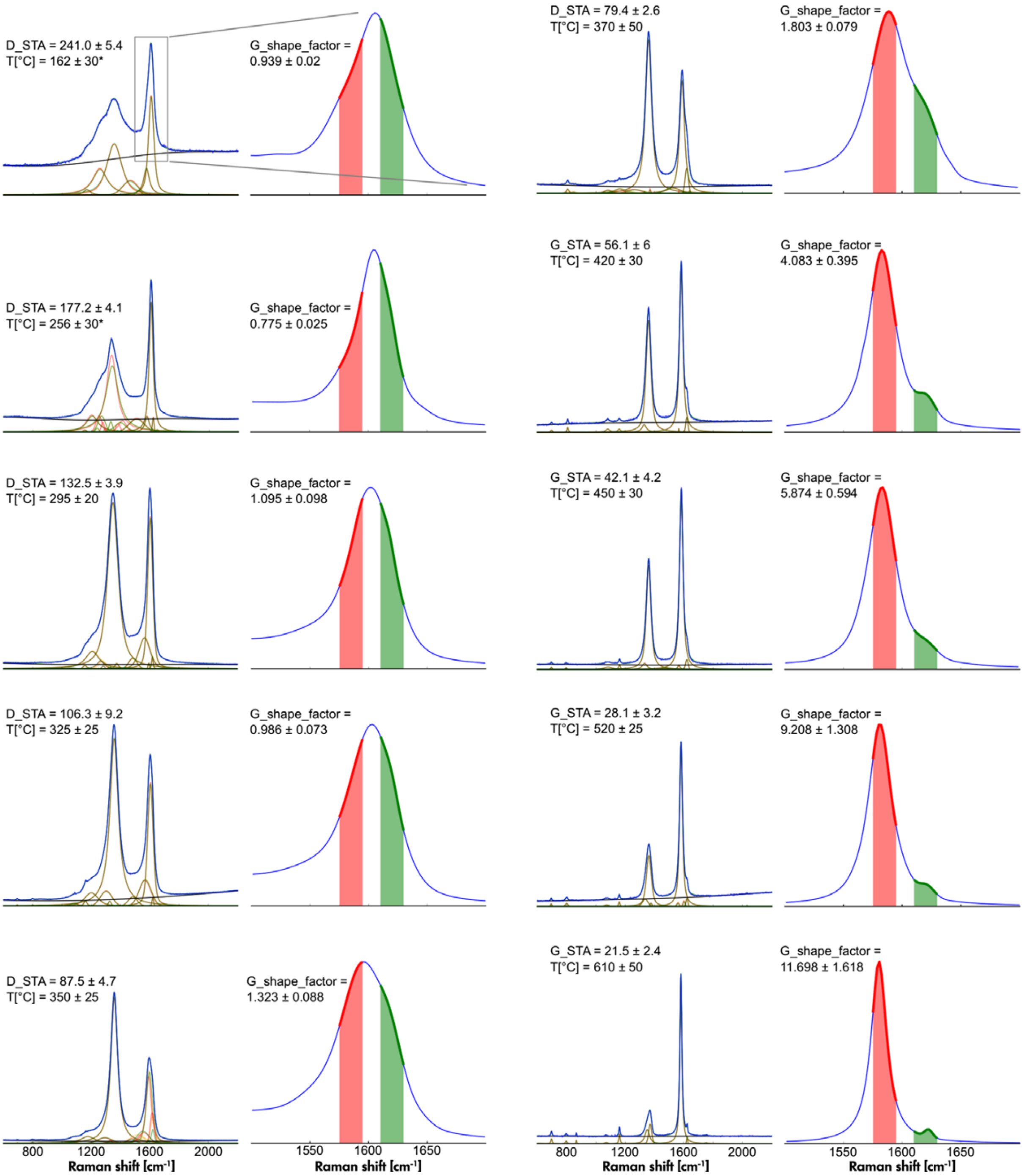

Figure 10. Selected examples that demonstrate the intensity distribution in the G-band-region of the CM Raman spectrum during maturation and graphitization, that is, the evolution of the G-shape-factor. [Colour figure can be viewed at wileyonlinelibrary.com]

They indicate no significant differences. The correlation between STA and metamorphic temperature for the 488 and 532 nm laser is shown in Figure 11c, d. A linear model is insufficient to describe the trend and a third-order polynomial was chosen to account for the different slopes of STA at temperatures below *ca.* 250 °C and in the high-temperature zone. Weighted orthogonal distance regression (Boggs *et al.* 1988, 1992) was used to determine the coefficients of the polynomials (Equations 4 and 5) and to account for the uncertainties in

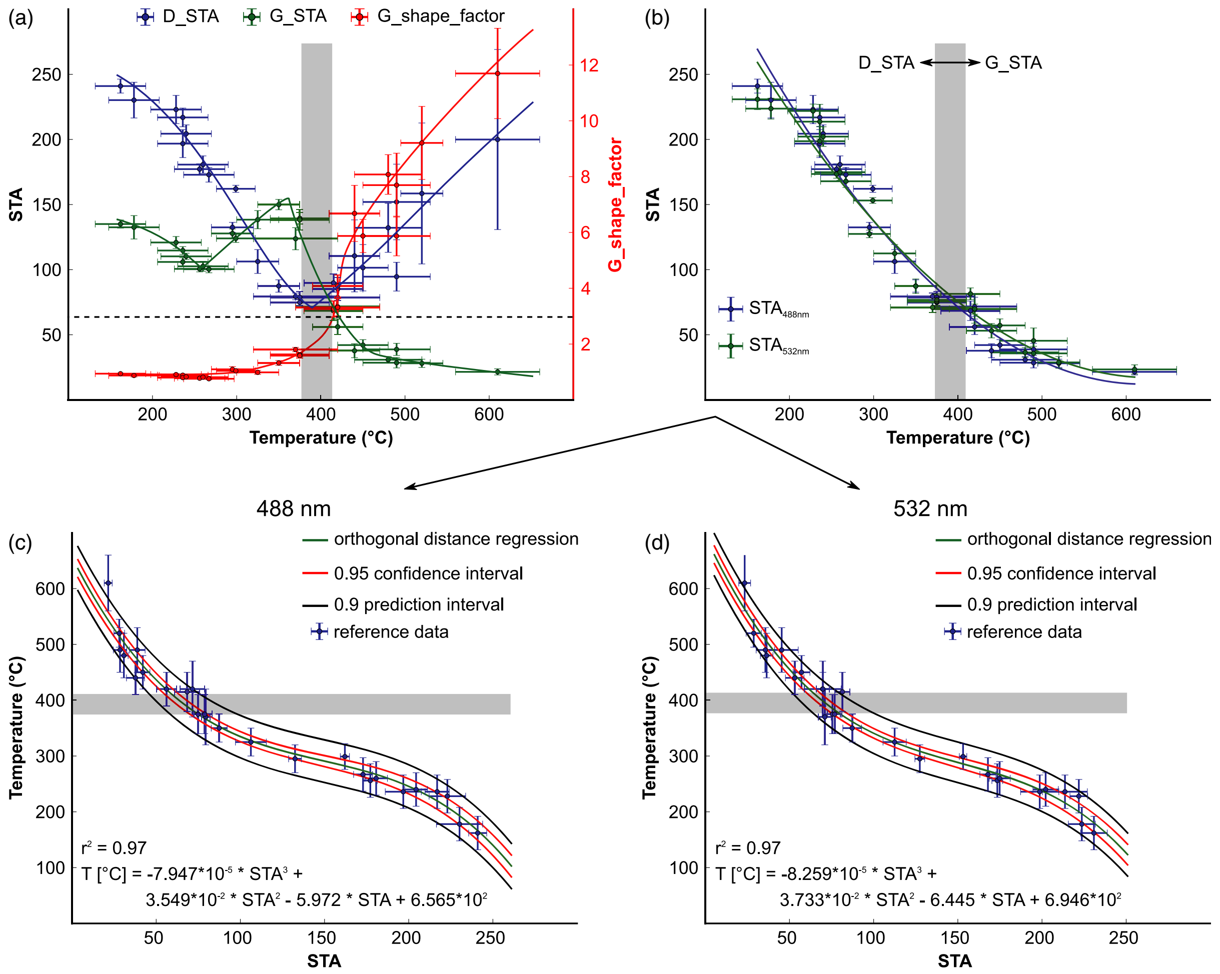

Figure 11. (a) A plot of D_STA, G_STA and the G-shape-factor. Until the end of the transition zone (marked by grey bar), D_STA decreases and G_STA shows varying values. After the transition zone D_STA increases, showing increasing spread of values, while G_STA decreases with significantly less scattered values. The G-shape-factor rapidly increases after the transition zone and values greater than 3 (stippled line) mark the end of the transition zone. (b) Because the G-shape-factor identifies the end of the transition zone, it allows to connect G_STA to D_STA. The combined STA values continuously decrease with peak metamorphic temperature from *ca.* 160 to 600 °C, and similar trends are observed for STA_{488nm} and STA_{532nm}. (c) Known metamorphic temperature plotted against STA_{488nm}. The trend shows different slopes and is described by a third-order polynomial. The coefficients of the polynomial were derived by orthogonal distance regression. (d) Same as (c) but the sample series was measured with a 532-nm wavelength laser. [Colour figure can be viewed at wileyonlinelibrary.com]

both variables, that is, temperature and STA; see Table 1.

$$T_{488\,\mathrm{nm}}[^{\circ}\mathrm{C}] = -7.947 * 10^{-5} * \mathrm{STA}^{3} + 3.549 * 10^{-2} * \mathrm{STA}^{2} - 5.972 * \mathrm{STA} + 6.565 * 10^{2} \quad (4)$$

$$T_{532\,\mathrm{nm}}[^{\circ}\mathrm{C}] = -8.259 * 10^{-5} * \mathrm{STA}^{3} + 3.733 * 10^{-2} * \mathrm{STA}^{2} - 6.445 * \mathrm{STA} + 6.946 * 10^{2} \quad (5)$$

where STA refers to scaled total area. The reference to the value used for scaling (D_{max} or G_{max}) has been omitted since both parameters (G_STA, D_STA) were used during regression. Based on a 90% confidence level, an uncertainty of *ca.* ± 40 °C is assigned to temperature values predicted from Equations 4 and 5 (Figure 11c, d). This uncertainty is in agreement with values reported in Beyssac *et al.* (2002) and Aoya *et al.* (2010).

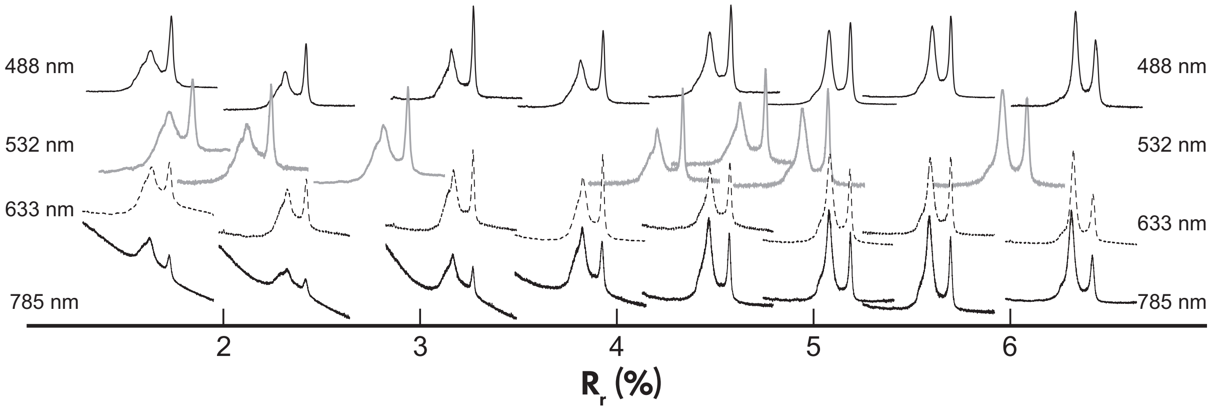

Figure 12. Raman spectra of CM, acquired with different excitation wavelengths (after figure 9a of Lünsdorf and Lünsdorf 2016), from very low-grade metamorphic to lower greenschist facies conditions (indicated by random vitrinite reflectance R_r). Although the spectra are of different shape, the general evolution with increasing metamorphism is comparable. Note the pronounced baseline increase with increasing excitation wavelength for the very low-grade metamorphic samples.

The proposed STA-RSCM method can be used as a geothermometer when a 488-nm or 532-nm laser is used, and will also work with other wavelengths, because the general spectral evolution is similar for different lasers (Figure 12). However, the G-shape-factor will probably need adjustment according to the used wavelength, because the position of the D′-band is wavelength dependent and shows a dispersion of *ca.* 10 cm^{-1} eV^{-1} (Pimenta *et al.* 2007). Thus, if a 633-nm laser is used, the excitation energy is decreased by 0.58 eV, compared with 488 nm, and the D′-band would downshift by *ca.* 6 cm^{-1} which results in a D′-band interval of *ca.* 1604–1624 cm^{-1}.

Comparison with other RSCM geothermometers

The RSCM geothermometers of Rahl *et al.* (2005) and Kouketsu *et al.* (2014) are compared with the STA_{532nm}-RSCM geothermometer (termed from here on T-STA) because the Raman spectra of these thermometers were acquired with a 532-nm laser and they cover similar temperature intervals. Rahl *et al.* (2005) covers 100–700 °C, Kouketsu *et al.* (2014) 165–655 °C and T-STA_{532nm} 160–600 °C. In the approach of Kouketsu *et al.* (2014), the decrease in FWHM of the D1 function is correlated with the increasing metamorphic temperature and the FWHM-D1 is determined by choosing one of seven curve-fitting approaches. The choice of the curve-fitting approach is guided by a flowchart that is based on differences in the general shape of the CM spectra (see figure 3 in Kouketsu *et al.* 2014).

The method of Kouketsu *et al.* (2014) is valid for temperatures below *ca.* 400 °C and extended by the geothermometer after Aoya *et al.* (2010). Rahl *et al.* (2005) fitted all CM spectra with four Voigt functions and fitted the combined changes in the R1- and R2 ratio to the metamorphic temperature using a bivariate polynomial function.

The three geothermometers are compared in Figure 13a. It is evident that temperatures estimated by T-$STA_{532\ nm}$ are similar to temperatures estimated according to Kouketsu *et al.* (2014). However, with 563 °C ± 50 (T after Kouketsu *et al.* 2014) and ± 17 (T-$STA_{532\ nm}$) both methods underestimate the metamorphic temperature of sample KL14_49, which is 610 ± 50 °C. The temperature estimates after Rahl *et al.* (2005) disagree with the temperatures; especially below *ca.* 400 °C, large differences become evident. This is due to the curve-fitting approach of Rahl *et al.* (2005), which does frequently not converge, and to the assignment of temperatures to CM spectra by Rahl *et al.* (2005).

The advantage of the T-STA method compared with the geothermometers of Beyssac *et al.* (2002), Aoya *et al.* (2010) and Lahfid *et al.* (2010) is its consistency over a large temperature range (160–600 °C). The others are only valid for either temperatures > 330 °C (Beyssac *et al.* 2002) and 340 °C (Aoya *et al.* 2010) or < 320 °C (Lahfid *et al.* 2010).

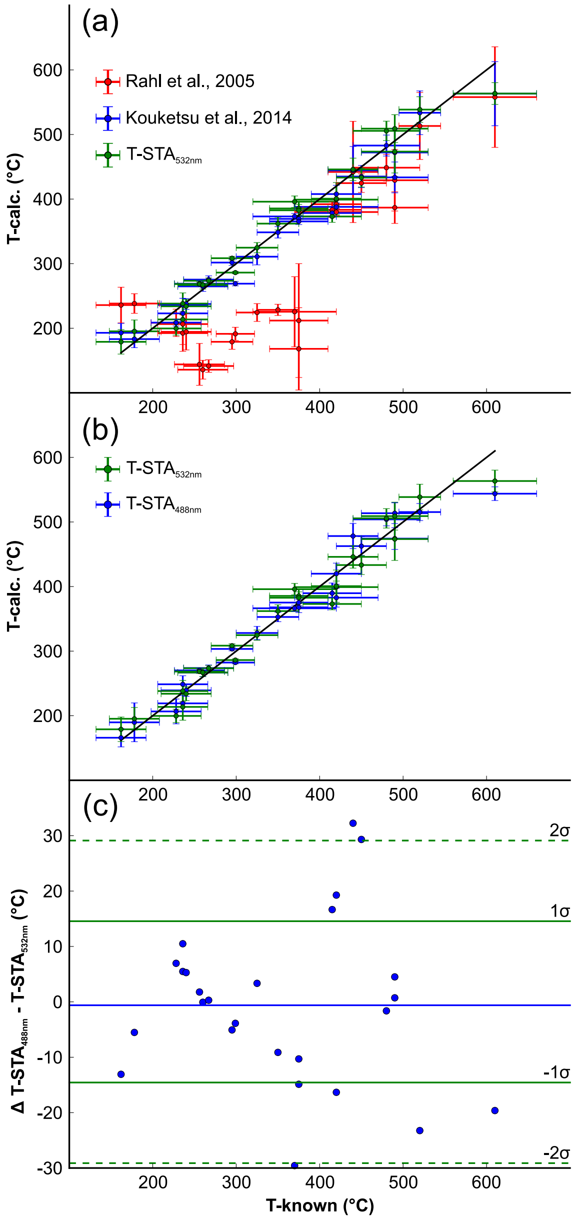

Figure 13. (a) Comparison of known metamorphic temperatures (T-known) with temperatures calculated (T-calc.) from different empirical geothermometers after Rahl *et al.* (2005), Kouketsu *et al.* (2014) and T-STA$_{532nm}$. (b) Comparison of T-STA$_{488nm}$ and T-STA$_{532nm}$. (c) Residuals between temperatures estimated by T-STA$_{488nm}$ and T-STA$_{532nm}$. [Colour figure can be viewed at wileyonlinelibrary.com]

Although the approach of Kouketsu *et al.* (2014) provides similar results, the user-guided choice of curve-fitting strategy introduces subjectivity and renders the method comparatively slow due to the constant manual intervention.

Figure 13b, c show that T-STA$_{488\ nm}$ and T-STA$_{532\ nm}$ are similar with a spread of ± 30 °C. This residual error is most likely related to within-sample heterogeneity, which gives rise to minor differences in the coefficients of the polynomials (see Equations 1 and 2). A similar residual error in T-STA is expected when other excitation wavelengths are used.

STA-RSCM protocol

To increase the certainty of temperature estimates from RSCM, a methodical protocol (STA-RSCM) is proposed for an objective evaluation of CM spectra.

- Preparation of polished rock fragments from samples that experienced very low- to low-grade metamorphism:
  - Cut the rock samples perpendicular to bedding and embed them in the usual resin mount.
  - Grind the samples using emery paper and polish them in several steps with diamond suspension on a hard polishing cloth to avoid relief. The finest diamond suspension cannot be finer than 1 µm (see Lünsdorf 2016 for details).
- Preparation of polished thin sections from samples of greenschist/blueschist and higher metamorphic overprint:
  - Prepare the samples by multi-step polishing for Raman analysis of CM below transparent, rock-forming minerals (follow the instructions given in, e.g., Beyssac *et al.* 2002).
- Measurement:
  - It is advised to use a blue or near UV excitation wavelength in order to reduce the fluorescence and increase the Raman signal of low mature CM.
  - When analysing polished rock fragments of low-grade samples, consider the maceral type and measure the Raman signal of vitrinite particles (Taylor 1998) whenever possible.
  - When analysing thin sections, avoid sheared/strained zones.
  - Try to analyse thirty particles, fifty if possible (Aoya *et al.* 2010).
  - Avoid photo-bleaching or thermal destruction of the CM by attenuating the laser power.
  - For proper baseline modelling, make sure that enough baseline is present in the spectrum; for CM, a spectral range from 400 to 2200 cm^{-1} is sufficient. If this range does not fit into one spectral window, use the extended range acquisition mode.

- Evaluation:
  - To exclude operator bias and to apply the proposed geothermometer, use the IFORS software (Lünsdorf and Lünsdorf 2016) to curve-fit CM Raman spectra. IFORS is available upon request from the first author or can be downloaded from: http://www.sediment.uni-goettingen.de/download/
  - If any parameters are changed in IFORS for a customised curve fitting, report the changed parameters.
  - If Raman bands of additional phases are present in the spectrum, exclude these bands before computing the results by indicating their Raman shift intervals.
- Calibration:
  - Measure and evaluate CM Raman spectra from reference samples, following the above protocol. The described reference series is available upon request from the first author.
  - Use the orthogonal distance regression script of the IFORS software on your STA and temperature values to generate a calibration line specific to your laboratory.

Opposed to the current practice to reuse a published calibration line, the proposed STA-RSCM method allows any laboratory to create its own specific calibration curve for RSCM geothermometry. In this way, effects of the measuring conditions bias (Lünsdorf *et al.* 2014), especially the effect of different excitation wavelengths, on the RSCM temperatures is omitted and the spectral processing bias (Lünsdorf *et al.* 2014), including the operator bias is excluded. To advance the method further and to increase the quality of the reference series, the scientific community is encouraged to extend the series with additional samples.

Conclusions

This study introduces a reference series of CM-bearing rock fragments that experienced a maximum thermal overprint between 160 and 600 °C determined by independent methods. This sample series is available from the first author on request and is supposed to be extended and refined by the scientific community. On the basis of this sample series, a methodological protocol has been established that will help to increase the overall comparability of temperature information derived from RSCM analysis. Using the automated curve-fitting software (Lünsdorf and Lünsdorf 2016), the spectral processing bias (Lünsdorf *et al.* 2014) can be reduced significantly. The measuring condition's bias, which is primarily due to the usage of different excitation wavelengths (Lünsdorf *et al.* 2014), can also be reduced by using the reference sample series to calibrate the STA-RSCM geothermometer for each laboratory individually.

Acknowledgements

The authors thank Martin Engi (Bern) and Meinert Rahn (ENSI) for advice on sampling localities and strategies. Volker Karius (Göttingen) is thanked for his assistance during XRD measurements and Andreas Kronz (Göttingen) for his assistance during EMP measurements. Finally, Ontje Lünsdorf is thanked for providing programming expertise. This project was supported by the Deutsche Forschungsgemeinschaft (DFG), grant number DU378/8-1.

References

Agard P., Jolivet L. and Goffé B. (2001a)
Tectonometamorphic evolution of the Schistes Lustres Complex: Implications for the exhumation of HP and UHP rocks in the Western Alps. **Bulletin de la Société Géologique de France**, **172**, 617–636.

Agard P., Vidal O. and Goffé B. (2001b)
Interlayer and Si content of phengite in HP-LT carpholite-bearing metapelites. **Journal of Metamorphic Geology**, **19**, 479–495.

Agard P., Monié P., Jolivet L. and Goffé B. (2002)
Exhumation of the Schistes Lustrés complex: *In situ* laser probe ^{40}Ar/^{39}Ar constraints and implications for the Western Alps. **Journal of Metamorphic Geology**, **20**, 599–618.

Ammar M.R. and Rouzaud J.-N. (2012)
How to obtain reliable structural characterization of polished graphitized carbons by Raman microspectroscopy. **Journal of Raman Spectroscopy**, **43**, 207–211.

Anovitz L.M. and Essene E.J. (1987)
Phase equilibria in the system $CaCO_3$-$MgCO_3$-$FeCO_3$. **Journal of Petrology**, **28**, 389–414.

Aoya M., Kouketsu Y., Endo S., Shimizu H., Mizukami T., Nakamura D. and Wallis S. (2010)
Extending the applicability of the Raman carbonaceous-material geothermometer using data from contact metamorphic rocks. **Journal of Metamorphic Geology**, **28**, 895–914.

references

Barzoi S.C. (2015)
Shear stress in the graphitization of carbonaceous matter during the low-grade metamorphism from the northern Parang Mountains (South Carpathians) – Implications to graphite geothermometry. International Journal of Coal Geology, 146, 179–187.

Beyssac O., Goffé B., Chopin C. and Rouzaud J.-N. (2002)
Raman spectra of carbonaceous material in metasediments: A new geothermometer. Journal of Metamorphic Geology, 20, 859–871.

Beyssac O., Goffé B., Petitet J.-P., Froigneux E., Moreau M. and Rouzaud J.-N. (2003)
On the characterization of disordered and heterogeneous carbonaceous materials by Raman spectroscopy. Spectrochimica Acta A, 59, 2267–2276.

Beyssac O., Simoes M., Avouac J.P., Farley K.A., Chen Y.G., Chan Y.C. and Goffé B. (2007)
Late Cenozoic metamorphic evolution and exhumation of Taiwan. Tectonics, 26, TC6001.

Boggs P.T., Spiegelman C.H., Donaldson J.R. and Schnabel R.B. (1988)
A computational examination of orthogonal distance regression. Journal of Econometrics, 38, 169–201.

Boggs P.T., Byrd R.H., Rogers J.E. and Schnabel R.B. (1992)
User's reference guide for ODRPACK version 2.01 software for weighted orthogonal distance regression. Center for Computing and Applied Mathematics, US Department of Commerce (Gaithersburg, MD), NISTIR 4834.

Bousquet R., Goffé B., Vidal O., Oberhänsli R. and Patriat M. (2002)
The tectono-metamorphic history of the Valaisan domain from the Western to the Central Alps: New constraints on the evolution of the Alps. Geological Society of America Bulletin, 114, 207–225.

Bustin R., Ross J. and Rouzaud J.-N. (1995)
Mechanisms of graphite formation from kerogen: Experimental evidence. International Journal of Coal Geology, 28, 1–36.

Castiglioni C., Tommasini M. and Zerbi G. (2004)
Raman spectroscopy of polyconjugated molecules and materials: Confinement effect in one and two dimensions. Philosophical Transactions of the Royal Society of London A, 362, 2425–2459.

Cathelineau M. (1988)
Cation site occupancy in chlorites and illites as a function of temperature. Clay Minerals, 23, 471–485.

Crespo E., Luque F.J., Barrenechea J.F. and Rodas M. (2006)
Influence of grinding on graphite crystallinity from experimental and natural data: Implications for graphite thermometry and sample preparation. Mineralogical Magazine, 70, 697–707.

Dachs E. (1990)
Geothermobarometry in metasediments of the southern Grossvenediger area (Tauern Window, Austria). Journal of Metamorphic Geology, 8, 217–230.

Deville E., Fudral S., Lagabrielle Y., Marthaler M. and Sartori M. (1992)
From oceanic closure to continental collision: A synthesis of the Schistes Lustrés metamorphic complex of the Western Alps. Geological Society of America Bulletin, 104, 127–139.

Ebert A., Herwegh M. and Pfiffner A. (2007)
Cooling induced strain localization in carbonate mylonites within a large-scale shear zone (Glarus thrust, Switzerland). Journal of Structural Geology, 29, 1164–1184.

Essene E.J. (1983)
Solid solution and solvi among metamorphic carbonates with applications to geologic thermobarometry. Reviews in Mineralogy and Geochemistry, 11, 77–96.

Ferrari A.C. and Robertson J. (2001)
Resonant Raman spectroscopy of disordered, amorphous, and diamond-like carbon. Physical Review B, 64, 075414.

Frey M. (1987a)
Low temperature metamorphism. Blackie (Glasgow, London), 351pp.

Frey M. (1987b)
The reaction-isograd kaolinite + quartz = pyrophyllite + H_2O, Helvetic Alps, Switzerland. Schweizerische Mineralogische und Petrographische Mitteilungen, 67, 1–11.

Frey M. and Ferreiro Mählmann R. (1999)
Alpine metamorphism of the Central Alps. Schweizerische Mineralogische und Petrographische Mitteilungen, 79, 135–154.

Hinrichs R., Brown M.T., Vasconcellos M.A., Abrashev M.V. and Kalkreuth W. (2014)
Simple procedure for an estimation of the coal rank using micro-Raman spectroscopy. International Journal of Coal Geology, 136, 52–58.

Kelemen S.R. and Fang H.L. (2001)
Maturity trends in Raman spectra from kerogen and coal. Energy and Fuels, 15, 653–658.

Kouketsu Y., Mizukami T., Mori H., Endo S., Aoya M., Hara H., Nakamura D. and Wallis S. (2014)
A new approach to develop the Raman carbonaceous material geothermometer for low-grade metamorphism using peak width. Island Arc, 23, 33–50.

Lahfid A., Beyssac O., Deville E., Negro F., Chopin C. and Goffé B. (2010)
Evolution of the Raman spectrum of carbonaceous material in low-grade metasediments of the Glarus Alps (Switzerland). Terra Nova, 22, 354–360.

Lemoine M., Bas T., Arnaud-Vanneau A., Arnaud H., Dumont T., Gidon M., Bourbon M., de Graciansky P.-C., Rudkiewicz J.-L., Megard-Galli J. and Tricart P. (1986)
The continental margin of the Mesozoic Tethys in the Western Alps. Marine and Petroleum Geology, 3, 179–199.

references

Li X., Hayashi J.-I. and Li C.-Z. (2006)
FT-Raman spectroscopic study of the evolution of char structure during the pyrolysis of a Victorian brown coal. Fuel, 85, 1700–1707.

Liu D.H., Xiao X.M., Tian H., Min Y.S., Zhou Q., Cheng P. and Shen J.G. (2013)
Sample maturation calculated using Raman spectroscopic parameters for solid organics: Methodology and geological applications. Chinese Science Bulletin, 58, 1285–1298.

Lünsdorf N.K. (2016)
Raman spectroscopy of dispersed vitrinite – Methodical aspects and correlation with reflectance. International Journal of Coal Geology, 153, 75–86.

Lünsdorf N.K. and Lünsdorf J.O. (2016)
Evaluating Raman spectra of carbonaceous matter by automated, iterative curve-fitting. International Journal of Coal Geology, 160–161, 51–62.

Lünsdorf N.K., Dunkl I., Schmidt B.C., Rantitsch G. and von Eynatten H. (2014)
Towards a higher comparability of geothermometric data obtained by Raman spectroscopy of carbonaceous material. Part 1: Evaluation of biasing factors. Geostandards and Geoanalytical Research, 38, 73–94.

Matthews M.J., Pimenta M.A., Dresselhaus G., Dresselhaus M.S. and Endo M. (1999)
Origin of dispersive effects of the Raman D band in carbon materials. Physical Review B, 59, R6585–R6588.

Pfiffner O.A. (2010)
Geologie der Alpen (2nd edition). Haupt Verlag (Bern, Stuttgart, Wien), 360pp.

Pimenta M.A., Dresselhaus G., Dresselhaus M.S., Cancado L.G., Jorio A. and Saito R. (2007)
Studying disorder in graphite-based systems by Raman spectroscopy. Physical Chemistry Chemical Physics, 9, 1276–1291.

Pócsik I., Hundhausen M., Koós M. and Ley L. (1998)
Origin of the D peak in the Raman spectrum of microcrystalline graphite. Journal of Non-Crystalline Solids, 227–230, 1083–1086.

Quirico E., Montagnac G., Rouzaud J.-N., Bonal L., Bourot-Denise M., Duber S. and Reynard B. (2009)
Precursor and metamorphic condition effects on Raman spectra of poorly ordered carbonaceous matter in chondrites and coals. Earth and Planetary Science Letters, 287, 185–193.

Rahl J.M., Anderson K.M., Brandon M.T. and Fassoulas C. (2005)
Raman spectroscopic carbonaceous material thermometry of low-grade metamorphic rocks: Calibration and application to tectonic exhumation in Crete, Greece. Earth and Planetary Science Letters, 240, 339–354.

Rahn M. (1996)
Incipient metamorphism of the Glarus Alps: Petrology of the Taveyanne Greywacke and fission track dating. PhD thesis, Albert-Ludwigs-Universität Freiburg.

Rantitsch G., Grogger W., Teichert C., Ebner F., Hofer C., Maurer E.-M., Schaffer B. and Toth M. (2004)
Conversion of carbonaceous material to graphite within the Greywacke Zone of the Eastern Alps. International Journal of Earth Sciences, 93, 959–973.

Rantitsch G., Lämmerer W., Fisslthaler E., Mitsche S. and Kaltenböck H. (2016)
On the discrimination of semi-graphite and graphite by Raman spectroscopy. International Journal of Coal Geology, 159, 48–56.

Reich S. and Thomsen C. (2004)
Raman spectroscopy of graphite. Philosophical Transactions of the Royal Society of London A, 362, 2271–2288.

Sadezky A., Muckenhuber H., Grothe H., Niessner R. and Pöschl U. (2005)
Raman microspectroscopy of soot and related carbonaceous materials: Spectral analysis and structural information. Carbon, 43, 1731–1742.

Scharf A., Handy M.R., Ziemann M.A. and Schmid S.M. (2013)
Peak-temperature patterns of polyphase metamorphism resulting from accretion, subduction and collision (eastern Tauern window, European alps) – A study with Raman microspectroscopy on carbonaceous material (RSCM). Journal of Metamorphic Geology, 31, 863–880.

Steinmann M. (1994)
Ein Beckenmodell für das Nordpenninikum der Ostschweiz. Jahrbuch der Geologischen Bundesanstalt, 137, 675–721.

Swisstopo (2005)
Tectonic map of Switzerland (1:500000). Geological Institute, University of Bern and Federal Office for Water and Geology. ISBN 3-906723-56-9.

Taylor G.H. (1998)
Organic petrology: A new handbook incorporating some revised parts of Stach's Textbook of coal petrology. Gebrueder Borntraeger (Berlin, Stuttgart), 704pp.

Todd C.S. and Engi M. (1997)
Metamorphic field gradients in the Central Alps. Journal of Metamorphic Geology, 15, 513–530.

Tuinstra F. and Koenig J.L. (1970)
Raman spectrum of graphite. The Journal of Chemical Physics, 53, 1126–1130.

references

Vidano R.P., Fischbach D.B., Willis L.J. and Loehr T.M. (1981)
Observation of Raman band shifting with excitation wavelength for carbons and graphites. **Solid State Communications**, **39**, 341–344.

Wang Y., Alsmeyer D.C. and McCreery R.L. (1990)
Raman spectroscopy of carbon materials: Structural basis of observed spectra. **Chemistry of Materials**, **2**, 557–563.

Wiederkehr M., Bousquet R., Schmid S.M. and Berger A. (2008)
From subduction to collision: Thermal overprint of HP/LT meta-sediments in the north-eastern Lepontine Dome (Swiss Alps) and consequences regarding the tectono-metamorphic evolution of the Alpine orogenic wedge. **Swiss Journal of Geosciences**, **101 (Suppl. 1)**, S127–S155.

Wiederkehr M., Sudo M., Bousquet R., Berger A. and Schmid S.M. (2009)
Alpine orogenic evolution from subduction to collisional thermal overprint: The ^{40}Ar/^{39}Ar age constraints from the Valaisan Ocean, Central Alps. **Tectonics**, **28**, TC6009, 1–28.

Wiederkehr M., Bousquet R., Ziemann M.A., Berger A. and Schmid S.M. (2011)
3-D assessment of peak-metamorphic conditions by Raman spectroscopy of carbonaceous material: An example from the margin of the Lepontine dome (Swiss Central Alps). **International Journal Earth Sciences**, **100**, 1029–1063.

Wilkins R.W.T., Boudou R., Sherwood N. and Xiao X. (2014)
Thermal maturity evaluation from inertinites by Raman spectroscopy: The 'RaMM' technique. **International Journal of Coal Geology**, **128–129**, 143–152.

Wopenka B. and Pasteris J.D. (1993)
Structural characterization of kerogens to granulite-facies graphite – Applicability of Raman microprobe spectroscopy. **American Mineralogist**, **78**, 533–557.

Yui T.-F., Huang E. and Xu J. (1996)
Raman spectrum of carbonaceous material: A possible metamorphic grade indicator for low-grade metamorphic rocks. **Journal of Metamorphic Geology**, **14**, 115–124.